Journal Pre-proofs

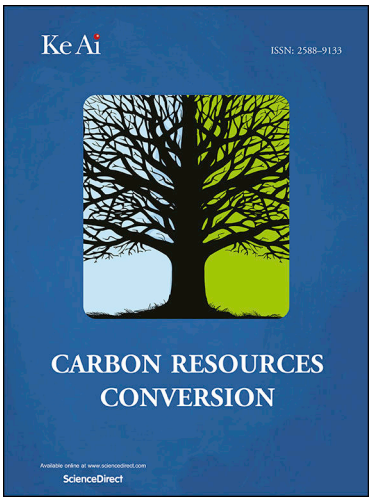

Original Article

Semi-industrial CO and CO_2 conversion with biochar-supported Fe-based catalysts

Mohammed H. Eldesouki, Mohamed Mokhtar Mohamed, Ahmed Abd El-Moneim

PII: S2588-9133(25)00056-0
DOI: https://doi.org/10.1016/j.crcon.2025.100358
Reference: CRCON 100358

To appear in: *Carbon Resources Conversion*

Received Date: 11 January 2025
Revised Date: 24 March 2025
Accepted Date: 20 July 2025

Please cite this article as: M.H. Eldesouki, M.M. Mohamed, A.A. El-Moneim, Semi-industrial CO and CO_2 conversion with biochar-supported Fe-based catalysts, *Carbon Resources Conversion* (2025), doi: https://doi.org/10.1016/j.crcon.2025.100358

Semi-Industrial CO and CO_2 Conversion with Biochar-Supported Fe-Based Catalysts

Mohammed H. Eldesouki*[a,b,c], Mohamed Mokhtar Mohamed[a,e], Ahmed Abd El-Moneim[a,c,d]

[a] Nano Science program, Basic and Applied Sciences Institute, Egypt-Japan University of Science and Technology, Borg Al Arab City, Alexandria 21934, Egypt.

[b] Petroleum Application Department, Egyptian Petroleum Research Institute, Nasr City, Cairo 11727, Egypt.

[C] Graphene Center of Excellence, Egypt-Japan University of Science and Technology, Borg Al Arab City, Alexandria 21934, Egypt.

[d] Physical Chemistry Department, National Research Centre, El-Doki, Cairo 12622, Egypt.

[e] Chemistry Department, Faculty of Science, Benha University, Benha, Egypt.

Corresponding author: Mohammed H. Eldesouki

Address: Basic and Applied Sciences Institute, Egypt-Japan University of Science and Technology, Borg Al Arab City, Alexandria, Egypt.

Email: mohammed.eldesouki@ejust.edu.eg

Abstract

This research investigates the use of biochar derived from agricultural waste as a support material for Fe-based (Fe-Co-K) catalysts, with and without Zn, in CO and CO_2 hydrogenation, benchmarking its performance against commercial activated carbon. Under semi-industrial Fischer-Tropsch conditions, biochar-supported catalysts, particularly the Zn-enhanced variant (ZFCK@C), delivered superior catalytic outcomes. The catalysts were prepared using ultrasound-assisted dissolution and incipient wetness methods and characterized using FTIR, XRD, BET, H_2-TPR, CO_2-TPD, XPS, and TEM. In CO hydrogenation at 340 °C and 20 bar, ZFCK@C achieved a remarkable 97% conversion, with 32% longer hydrocarbons selectivity(C_{5+}), 39.6% olefins distribution(C_{5+}), an O/P ratio of 4.0, and 45.3% gasoline-range (C_5–C_{12}) hydrocarbons distribution. For CO_2 hydrogenation at 340 °C and 30 bar, the catalyst showed 40% conversion, low CH_4 selectivity (6.1%), high C_{5+} selectivity (45%), 38.7% olefins distribution(C_{5+}), an O/P ratio of 3.2, and 45.3% kerosene-range (C_6–C_{16}) hydrocarbons distribution. Stability testing over 100 h demonstrated excellent durability with no significant deactivation or sintering, making the catalyst viable for extended industrial use.

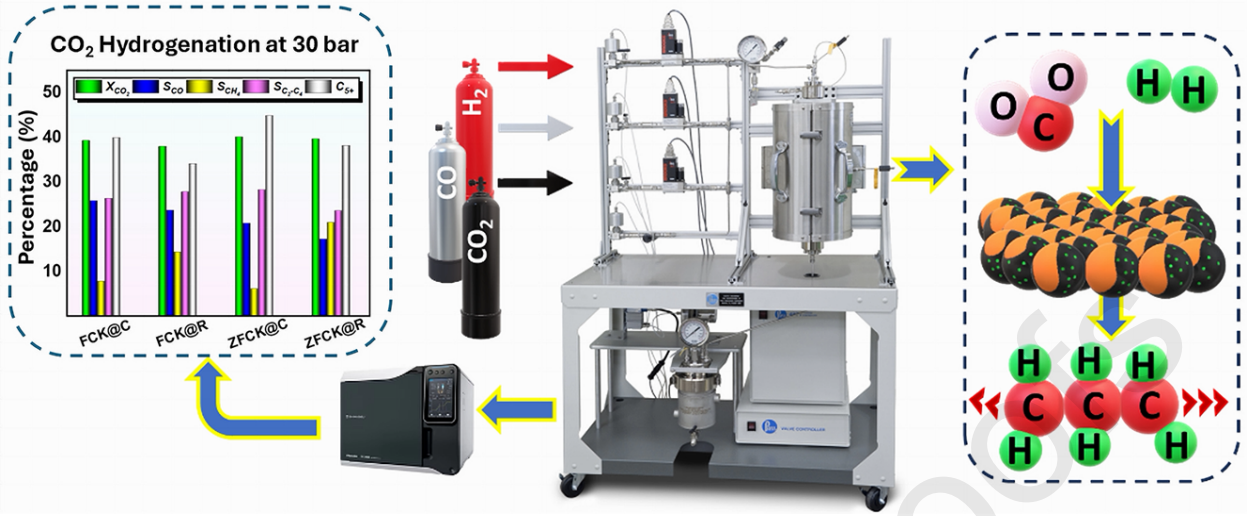

Graphical abstract

Keywords

CO conversion; CO_2 hydrogenation; Gasoline production; Fixed bed reactor; Carbonaceous supports

1. Introduction

CO and CO_2 are products of the combustion of carbon-containing materials, such as fossil fuels, but they differ significantly in their properties and impacts [1]. CO is a colorless, odorless gas resulting from incomplete combustion [2], while CO_2 is produced during complete combustion. Both gases have significant environmental and health impacts [3]. CO contributes to air pollution and poses immediate health risks [4], while CO_2 is a primary driver of long-term climate change. Strategies to combat these emissions include the development and implementation of carbon capture, usage, and storage (CCUS) technologies, which can capture CO_2 from industrial processes and power generation. It is estimated that approximately 95% of the total CO_2 captured in 2050 will be stored in permanent geological storage, with the remaining 5% converted to produce synthetic fuels. According to the International Energy Agency (IEA), achieving zero CO_2 emissions by 2050 requires a significant shift to sustainable energy and a reduction in the combustion of fossil fuels, which would also mitigate the production of CO [5]. This integrated approach underscores the interconnectedness of addressing CO and CO_2 emissions to protect human health and mitigate climate change.

Unlike CO, the hydrogenation of CO_2 poses a significant challenge due to the strong bond between carbon and oxygen, which informs the high stability of the gas. This requires employing rigorous conditions, including elevated pressure and temperature, to rupture the bond and enable the reaction to proceed [6]. Scientists have been developing catalysts capable of hydrogenating CO and CO_2 under adequate parameters including pressure, temperature, and GHSV. Among these catalysts, Fe-based catalysts stand out as one of the most widely used in the conversion processes of both CO [7] and CO_2 [8, 9]. To increase the effectiveness of the catalyst, materials with a high

surface area such as graphene [10], alumina [8], silica [11], MOF [12, 13], and carbonaceous materials [14-16] have been employed as support. Catalyst supports play a crucial role in enhancing catalytic activity and stability by preventing the agglomeration of Fe-active sites through the adhesion process [17, 18]. Moreover, these supports offer a large surface area, facilitating the interaction of molecules [19]. Additionally, scientists have introduced promoter metals such as alkali metals (e.g., Na [20, 21], K [22, 23], Li [24], Rb [24, 25], and Cs [26-28]), transition metals (e.g., Zr [29, 30], Zn [31, 32], Cu [33, 34], Co [35], Ni [36, 37], Ru [38] and Mg [39, 40]), and/or post-transition metals (e.g., Al [41, 42], Si [43] and Sn [44]) to improve the efficiency of the catalyst.

Carbonaceous materials play a significant role in catalytic processes due to their unique properties and surface characteristics [45-48]. As a highly porous material with a large surface area, biochar provides an excellent support structure for catalysts, allowing for enhanced dispersion and stabilization of active catalytic species. This promotes increased catalytic activity and selectivity in various chemical reactions. Moreover, the surface functional groups present in biochar, such as hydroxyl (-OH), carboxyl (-COOH), and phenolic (-OH) groups, can interact with catalytic species and substrates, facilitating adsorption and activation of reactant molecules. This interaction can lead to improved reaction kinetics and efficiency in catalytic processes [49]. Additionally, biochar's thermal stability and resistance to chemical degradation make it a durable support material for catalytic applications, ensuring long-term performance and recyclability of catalysts [50]. Furthermore, biochar's carbonaceous nature enables it to act as a reducing agent or source of carbon in certain catalytic reactions, thereby promoting specific reaction pathways and product formation [51].

This work looks at how the unique porosity architectures of biochar and activated carbon affect the catalytic efficiency of Fe-based catalysts in CO and CO_2 hydrogenation over a semi-industrial FTS reactor. The study focuses on crucial indicators including conversion rates, product selectivity, and hydrocarbons distribution. While previous research has shown that commercially available activated carbon is effective as a support material in CO_2 hydrogenation catalysts, this study takes a novel approach by using biochar derived from recycled agricultural waste, specifically corn cobs, as a carbonaceous support for Fe-based catalysts. By exploring the usage of biochar, the study seeks to gain useful insights into the function of support materials in catalyst design, with a special emphasis on sustainable and ecologically friendly catalytic processes for CO and CO_2 conversion. The study is carried out under actual reaction circumstances utilizing a semi-industrial 1-inch stainless steel fixed bed reactor, with practical implications and prospective applications in the field of renewable energy generation.

2. Experimental

2.1. Materials

The corn cobs utilized in this study were sourced from a local farm in Egypt, ensuring a readily available and sustainable feedstock for biochar. Potassium hydroxide (KOH, 99% purity), hydrochloric acid (HCl 37%), iron (III) nitrate nonahydrate ($Fe(NO_3)_3{\cdot}9H_2O$, 98% purity), zinc (II) acetate dihydrate ($Zn(CH_3COO)_2{\cdot}2H_2O$, 98% purity), cobalt (II) nitrate hexahydrate ($Co(NO_3)_2{\cdot}6H_2O$, 97% purity), potassium carbonate (K_2CO_3, anhydrous, 99% purity), activated

charcoal and absolute ethanol were procured from Sigma-Aldrich. These chemicals were utilized as received without further purification.

2.2. Preparation of Biochar from Corn cob

As illustrated in Fig. 1, the corn cob was washed with 0.1 M HCl, rinsed with distilled water until the pH was neutralized, dried at 100 °C and ground into small particles. The sample was then carbonized in a tube furnace under N_2 flow at 450 °C for 4 h, with a heating rate of 10 °C min^{-1}, followed by re-washing with 0.1 M HCl and distilled water until the pH was neutralized. Subsequently, it was dried in an oven at 80 °C overnight before being manually milled into a fine powder. The activation step was carried out by manually grinding the sample with KOH (1:1 wt.%). In a tube furnace, the calcination process was conducted at a temperature of 700 °C for 1 h, with a heating rate of 10 °C min^{-1} under N_2 flow. The final product was washed with 0.1 M HCl, followed by several rinses with distilled water until a neutral pH was achieved, and then dried at 100 °C overnight. The commercial activated carbon was used as received, without undergoing any additional treatment.

2.3. Catalyst Preparation

For the preparation of a 5 g catalyst, 17.0 mmol of iron nitrate nonahydrate was dissolved in an appropriate volume of ethanol using ultrasound-assisted dissolution filtration. Then 3.5 g of carbonaceous material was added and sonicated for 1 h. Subsequently, the solution was supplemented with 3.0 mmol of zinc and 2.0 mmol of cobalt precursors and sonicated for 5 h. The resulting solution was dried overnight in an oven at 85 °C. Following this, 3.0 mmol of potassium carbonate was loaded using an incipient wetness impregnation step. A catalyst without Zn was prepared similarly, utilizing 3.7 g of carbonaceous material. Finally, the catalyst was pyrolyzed at a temperature of 500 °C for 5 h at a rate of 10 °C min^{-1} under N_2 flow. The samples prepared using biochar were designated as ZFCK@C for samples containing Zn and FCK@C for samples free of Zn. The samples that were prepared using activated carbon were named FCK@R and ZFCK@R, respectively, for the Zn-free and Zn-containing samples respectively.

Fig. 1. Schematic illustration of the synthesis of the carbonaceous support and catalyst.

2.4. Catalyst Characterization

FTIR spectra were generated using a Bruker Vertex 70 to investigate chemical characteristics. X-ray diffraction (XRD) patterns were plotted using a Shimadzu XRD6100 with Cu-K radiation in the 2θ range of 20-80° to identify phases and crystallinity. The Debbye-Scherrer equation and MDI Jade software (version 6) were employed to determine crystal size. The N_2 adsorption isotherms were measured using a BEL Japan (BELSORP II mini) instrument. The data were analyzed using the Brunauer-Emmett-Teller (BET) and Barrett-Joyner-Halenda (BJH) t-plot methods to determine the BET surface area, total pore volume, and average pore diameter. Microtrac Bellcat II was used to measure H_2-Temperature-programmed reduction (H_2-TPR) and CO_2-Temperature programmed desorption (CO_2-TPD). The quartz reactor was loaded with 100 mg of sample for CO_2-TPD. The sample was treated with pure He at a flow rate of 50 ml min^{-1}, the temperature at a rate of 5 °C min^{-1}, and then the temperature was held at 200 °C for 30 min. Subsequently, the sample was reduced with pure H_2 at 400 °C for 4 h at a flow rate of 50 ml min^{-1} and then cooled to 50 °C under the flow of pure He for an hour. Next, a stream of 10 vol% CO_2/He at 50 ml min^{-1} was introduced for an hour, followed by pure He for 20 min. Finally, the temperature was raised to 850 °C at a rate of 10 °C min^{-1}, and the measurements were taken by the TCD detector after stabilization. For H_2-TPR, results were recorded at room temperature up to 850 °C while heating at a rate of 10 °C min^{-1} with a 50 ml min^{-1} stream of 10 vol% H_2/Ar. The surface chemistry was investigated using X-ray photoelectron spectroscopy (XPS) K-ALPHA (Thermo Fisher Scientific, USA) with monochromatic X-ray Al Kα radiation (-10 to 1350 eV), a spot size of 400 µm, and a pressure of 9-10 mbar with a full spectrum pass energy of 200 eV and a narrow spectrum pass energy of 50 eV. Transmission electron microscopy (TEM) images were collected using a JEOl 2100 Plus microscope to study the morphological structure, particle size distribution, and dispersion of the prepared materials.

2.5. Catalyst Loading

As depicted in Fig. 2 and Fig. 3, the assembly process of the reactor column commences with the insertion of a thermocouple into the column's center from the top, followed by tightly sealing the top with a designated part using anchor bolts. Subsequently, the column is inverted and securely fixed in a horizontal position using a clamp. A cylindrical metal piece, referred to as the catalyst support, is then positioned to accommodate the thermocouple. Glass beads are carefully poured into the column to fill the space up to a specified point in the middle where temperature concentration occurs. To separate the catalyst from the glass beads, glass wool is layered on the bottom of the glass beads. Following this, the catalyst is loaded into the column, with glass wool placed at the bottom of the catalyst to prevent its passage through the glass beads under pressure. Additional glass beads are added until the bottom of the column is filled, after which more glass wool is placed at the end of the column. Subsequently, the column is sealed from the bottom using a specialized component that permits gases and products to pass into the cold trap. Finally, the column is positioned inside the furnace, with the upper part connected to the gas supply pipeline for gas entry and the lower part linked to the cold trap to facilitate product collection.

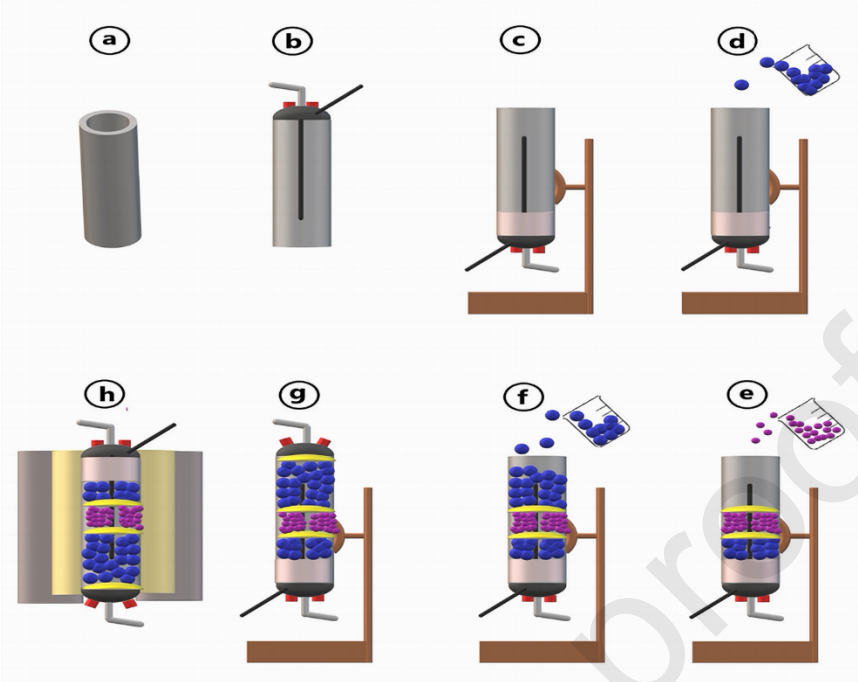

Fig. 2. Schematic illustration of catalyst loading: (a) rector column before filling, (b) thermocouple fixation and closure of the upper part, (c) turning over the column, (d) filling the upper part with glass beads, (e) catalyst loading, (f) filling the lower part with glass beads, (g) closure the lower part, and (h) fixation of the column inside the furnace.

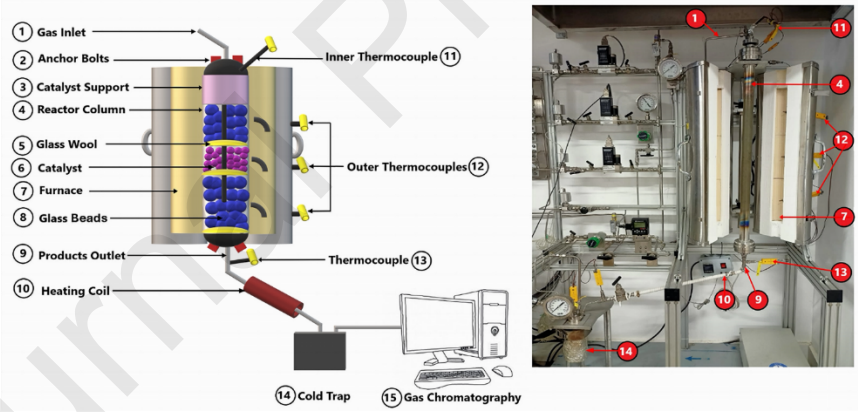

Fig. 3. Schematic and photographic images showing the components of the reactor.

2.6. Reactor Performance Evaluation

The CO_2 hydrogenation reaction was evaluated in a 1-inch stainless fixed-bed reactor, as shown in Fig. 3, (2.54 cm in diameter, 85 cm in length, a volume of 430 cm^3, and a loading capacity of up to 500 g of catalyst) containing 2.5 g of catalyst sample mixed with the same weight of SiC. Firstly, the samples were reduced in situ for 10 h in a flowing stream of pure H_2 (GHSV = 1700 mL g^{-1}_{cat} h^{-1}, T= 400 °C and under atmospheric pressure) and then cooled to 50 °C. For CO hydrogenation, the conditions included a H_2/CO=1.0 (molar ratio), GHSV = 3000 mL g^{-1}_{cat} h^{-1}, T = 340 °C and P = 20 bar. The catalytic reaction conditions of CO_2 hydrogenation were as follows: H_2/CO_2 = 3 (molar ratio), GHSV = 3000 mL g^{-1}_{cat} h^{-1}, T = 340 °C and P = 20 and 30 bar. A cold

trap filled with n-octane (2 g) for liquid hydrocarbon fraction collection, n-dodecane (0.1 g) as an internal standard for GC measurements, and H_2O (30 g) was used at 2 °C. The effluent gas was analyzed using an online gas chromatograph GC-2030 DHA SHIMADZU, model (Nexis GC-2030 AF), which was equipped with a TCD detector for C_1 product analysis (CO_2, CO and CH_4). The He carrier gas flow rate was 20 ml min^{-1}, heating the injection ports to 100 °C, the column to 120 °C, and the TCD detector to 150 °C. FID detector was used to detect C_1–C_8 gaseous hydrocarbon products. The collected hydrocarbon liquid was analyzed by an off-line gas chromatograph using FID detector. The results were analyzed by Dragon software using PIONA references where the percentage of paraffines, olefins, and iso-paraffins were recorded. The mass balance was based on carbon and the results were calculated in terms of activity for CO or CO_2 conversion and CH_4, light hydrocarbons (C_2-C_4), and high hydrocarbons (C_{5+}) selectivity. The conversion rate and product selectivity are defined as:

$$Conversion\ (\%) = 100 \times \frac{n\ C\ in - n\ C\ out}{n\ C\ in}$$

$$Selectivity\ (\%) = 100\ \times\ \frac{n\ product\ out\ \times carbon\ number}{n\ C\ in - n\ C\ out}$$

Where n is the number of moles and C refers to CO in the context of CO hydrogenation reactions or CO_2 in the context of CO_2 hydrogenation reactions.

3. Results and Discussion

3.1. Catalyst Characterization

Fig. 4a depicts the FTIR spectra of the FCK@C, FCK@R, ZFCK@C, and ZFCK@R samples. The spectra show a significant resemblance in functional groupings related to carbonaceous materials. The conspicuous band at 3447 cm^{-1} is due to the stretching vibration of hydroxyl groups (-OH) [52]. Furthermore, the band at 1637 cm^{-1} represents the stretching vibration of carbon-carbon double bonds (C=C) [53]. The peak at 1386 cm^{-1} corresponds to the stretching vibration of carbon-carbon bonds (C-C) [54]. Furthermore, a minor signal at 1118 cm^{-1} is most likely caused by the stretching vibration of carbon-oxygen bonds (C-O) [55]. The peak at 698 cm^{-1} represents the bending vibration of carbon-hydrogen bonds (C-H) [56] , especially that associated with the C=C bond structure. The shift of the OH stretching peak from 3447 cm^{-1} to lower wavenumbers in Zn-containing samples indicates that the mass increases due to the further insertion of Zn ions into the sample. This shift reflects alterations in the hydrogen bonding environment, which might be caused by enhanced contact between the Zn and OH groups. Zn-containing samples exhibit significant shoulders about 3600 cm^{-1} in the O-H stretching region. These shoulders most likely represent free OH groups that are less engaged in hydrogen bonding. This can happen when fewer linked or isolated clusters form within the sample, and the OH groups aren't as well networked as they would be in a more homogeneous material. The presence of Zn appears to disrupt the normal hydrogen bonding network [57], resulting in these unusual spectrum characteristics.

Fig. 4b, c displays the XRD patterns of catalysts in their fresh and spent states after CO_2 hydrogenation, highlighting notable structural changes. In the fresh forms (Fig. 4b), distinctive crystallographic planes (220), (311), (400), (511), and (440) reveal the presence of the maghemite

(γ-Fe_2O_3) phase (JCPDS No. 39-1346). Notably, biochar-supported catalysts display more intense peaks than those supported on activated carbon, indicating biochar's effectiveness in enhancing the distribution of active crystalline phases. Additionally, the Zn-containing catalyst (ZFCK@C) exhibits a stronger peak at $2\theta = 35.5°$ than the Zn-free sample, further supporting the role of Zn in promoting more intense Fe phase peaks, as observed by Gao, Zhang et al [58]. These results underscore the combined influence of biochar and Zn in optimizing the dispersion and distribution of Fe species. In the spent forms (Fig. 4c), peaks corresponding to magnetite (Fe_3O_4, JCPDS No. 19-0629) are observed at planes (311), (400), and (531), indicating a transformation from γ-Fe_2O_3 to Fe_3O_4. This conversion suggests a partial reduction of Fe^{3+} to Fe^{2+} during the CO_2 hydrogenation process. Additionally, in the Zn-containing samples, peaks at planes (100) and (110) correspond to ZnO nanoparticles. The Scherrer formula was utilized to calculate the average crystallite diameter, excluding SiC peaks. Generally, the Zn-containing samples exhibited smaller crystallite sizes compared to their Zn-free counterparts. In the fresh state, the average crystallite size of FCK@C was approximately 17.2 nm, while that of FCK@R was 19.1 nm. After the reaction, these sizes increased to 35.6 nm and 42.0 nm, respectively. In contrast, the fresh ZFCK@C crystals had a smaller average size of 12.5 nm, which grew to about 30.1 nm following the reaction. For ZFCK@R, the initial size was 17.5 nm, increasing to 38.7 nm post-reaction.

Using techniques like BET, H_2-TPR, and CO_2-TPD to evaluate surface area, porosity, reducibility, and CO_2 adsorption strength are excellent probes for understanding the structural and textural characteristics of catalysts for CO_2 adsorption and transformation. As shown in Fig. 4d ZFCK@C exhibits a type I isotherm with H4 hysteresis, indicating a microporous structure. In contrast, ZFCK@R exhibits a type II isotherm with H3 hysteresis, indicating a wider pore size distribution and bigger pore spaces (Fig. 4e). ZFCK@C has a greater specific surface area (587 m^2/g) than ZFCK@R (428 m^2/g), resulting in more active sites for improved CO_2 adsorption, as seen by the CO_2-TPD graph. Both samples have comparable total pore volumes, however, ZFCK@R has bigger pore apertures (3.07 nm) than ZFCK@C (2.04 nm). ZFCK@C also has a pronounced pore size distribution with peaks at 12 and 22 nm, while ZFCK@R shows a broader, less defined distribution, indicating mesoporosity in both samples. In summary, ZFCK@C's smaller pore size and higher surface area may contribute to its catalytic efficiency, than ZFCK@R.

The H_2-TPR analysis is essential for understanding the reduction behavior of catalyst samples, particularly in systems involving metal components and carbon-based supports. Fig. 4f highlights the H_2-TPR profiles for biochar- and activated carbon-supported catalysts, emphasizing Zn's key role in enhancing reducibility. Iron oxides generally undergo a two-step reduction: Fe_2O_3 reduces to Fe_3O_4 around 400 °C, followed by a reduction to metallic iron (Fe^0) above 500 °C [59]. In this study, catalysts supported on biochar showed lower reduction temperatures than those on activated carbon, suggesting that biochar promotes easier reduction, possibly due to better dispersion of Fe species or stronger interaction between Fe and biochar. For example, the Zn-free FCK@C catalyst exhibited two reduction peaks: Fe_2O_3 to Fe_3O_4 at 403 °C and Fe_3O_4 to Fe^0 at 560 °C. In contrast, the activated carbon-supported FCK@R had a higher reduction temperature of 585°C for the second stage. Zn incorporation significantly lowered reduction temperatures. For instance, ZFCK@R showed an initial reduction at 468 °C, far lower than FCK@R's 585 °C. In addition, ZFCK@C displayed three peaks: i) Fe_2O_3 to Fe_3O_4 at 370 °C, ii) partial reduction of Fe_3O_4 to FeO at 502 °C, and iii) reduction to Fe^0 at 583 °C. Two factors likely contribute to enhanced reduction in Zn-containing catalysts: i) ZnO's semiconductor properties, which facilitate electron transfer during reduction [60], and ii) smaller particle sizes, confirmed by TEM and XRD,

which are more easily reduced [61]. Regarding H_2 consumption, FCK@C, and ZFCK@C demonstrated higher rates (417 and 356 μmol H_2 g^{-1}, respectively) compared to the activated carbon-supported catalysts, as shown in Table S1. These findings suggest that the combination of biochar and Zn enhances reduction efficiency, likely due to the synergistic effects of biochar's catalytic properties and Zn's role in improving the reducibility of Fe species.

Fig. 4g illustrates the CO_2-TPD profiles of the catalysts, showing three distinct CO_2 desorption peaks for each sample. These peaks correspond to multiple types of basic sites with varying strengths—ranging from weak to strong interactions with CO_2. The presence of these peaks indicates a significant capacity for CO_2 adsorption across all catalysts. The inclusion of Zn generally shifts the desorption peaks to higher temperatures compared to the Zn-free catalysts, indicating enhanced interactions between CO_2 and the catalyst surface. However, it is noteworthy that not all desorption peaks follow this trend. For instance, ZFCK@C exhibits an initial CO_2 desorption peak at 536 °C, which is lower than the corresponding peak of FCK@C at 578 °C. Similarly, the last desorption peak for ZFCK@R occurs at a lower temperature than the equivalent peak for FCK@R. These exceptions suggest that Zn influences the interaction strength of CO_2 with the catalyst surface in a non-uniform manner, depending on the type and location of adsorption sites. Conversely, ZFCK@C's third peak appears at 763 °C, higher than FCK@C's peak at 716 °C, indicating that CO_2 chemically bound to the Zn-containing catalyst is held more tightly on specific sites. As confirmed by TEM and XRD analyses, Zn plays a critical role in reducing the particle size of the active Fe species, increasing the surface area and the number of active sites available for CO_2 adsorption [62]. This reduction in particle size, along with Zn's interaction with the support material, appears to enhance adsorption on certain sites, leading to higher desorption temperatures. However, the lower temperature desorption peaks observed for ZFCK@C and ZFCK@R compared to their Zn-free counterparts suggest that Zn may also alter weaker adsorption sites, reducing the binding strength in some cases. These findings emphasize the dual role of Zn in modifying the adsorption behavior of CO_2. While stronger adsorption, as seen at higher desorption temperatures, is beneficial for applications like CO_2 hydrogenation or dry reforming, it may also lead to slower desorption and potential challenges in catalytic transformation. Balancing these effects is critical for optimizing catalyst performance for specific reactions.

XPS measurement was used to comprehend the surface chemistry and disclose critical insights into the composition and alterations seen between the fresh and spent catalyst states of the ZFCK@C catalyst (Fig. 4h, i)**.** The XPS survey spectra show the presence of Zn, Fe, Co, K, C, and O in both fresh and used catalysts. The Fe 2p spectrum exhibits significantly split spin-orbit components, with a separation (Δmetal) of 13.1 eV. The area ratio of the two spin-orbit peaks, Fe $2p_{1/2}$ and Fe $2p_{3/2}$, is 1:2, corresponding to the electronic configurations of 2 electrons in the $2p_{1/2}$ level and 4 electrons in the $2p_{3/2}$ level. The Fe $2p_{3/2}$ and Fe $2p_{1/2}$ peaks were observed at around 711 eV and 725 eV, respectively [63, 64]. The presence of satellite peaks at 719.2 eV and 734.1 eV suggests the involvement of Fe in complex electronic environments, often seen in iron oxides or hydroxides [65]. These satellite peaks are generally associated with shake-up transitions of Fe in high-spin states, confirming iron's oxidation state and electronic structure. In the fresh ZFCK@C catalyst (Fig. 4h), the Fe $2p_{3/2}$ peak was deconvoluted into two components: a major peak at 711.3 eV, attributed to Fe^{2+} species, and a minor peak at 714.1 eV, associated with Fe^{3+} species [65]. Similarly, the Fe $2p_{1/2}$ peak was deconvoluted into two peaks at 724.5 eV and 727.2 eV, corresponding to the Fe-O bonds of Fe^{2+} and Fe^{3+}, respectively. In the spent catalyst (Fig. 4i),

the Fe $2p_{3/2}$ and Fe $2p_{1/2}$ peaks of iron oxide were deconvoluted into six distinct components. Peaks at 710.5 eV, 712.5 eV, 722.2 eV, and 724.9 eV were assigned to the Fe-O bonds of Fe^{2+} ions, while peaks at 715.2 eV and 728.2 eV were attributed to the Fe-O bonds of Fe^{3+} ions in the Fe_3O_4 phase [66]. An increase in the proportion of Fe^{2+} species, coupled with a decrease in Fe^{3+} species, suggests the formation of Fe_3O_4, which is compatible with XRD data. The Zn 2p spectrum has two peaks at 1044.9 eV and 1021.8 eV, which correspond to Zn $2p_{1/2}$ and Zn $2p_{3/2,}$ respectively, indicating the presence of the Zn^{2+} state in the catalyst. The C 1s spectra in the fresh catalyst have three deconvoluted peaks at 284.1, 286.3, and 288.4 eV, which correspond to C=C, C-O, and C=O bonds, respectively [67-69], while, the two peaks that appeared at 293.2 and 296.2 eV were due to K 2p. The spent catalyst showed three peaks at 282.0, 284.1 and 285.5 eV that corresponded to Fe-CH_X, C=C, and C-C respectively [69-72]. These findings imply that Fe carbide species are formed during the reaction, which is accompanied by a decrease in oxygen species at the catalyst surface. The fresh catalyst's O 1s spectrum is fitted to two peaks at 530.5 and 532.18 eV, which are assigned to (C-O-Fe) and the oxygen in the adsorbed OH groups on the sample surface, respectively [73]. The spent catalyst exhibited two peaks at 530.1 and 531.6 eV which are attributed to Fe-O and oxygen defects in the matrix of metal oxides respectively [74]. In brief, the XPS results provide crucial insights into the oxidation states, surface bonding, and compositional changes in the ZFCK@C catalyst, particularly the transformation of iron and carbon species during catalyst use. When combined with XRD data, this XPS analysis offers a comprehensive understanding of the catalyst's behavior and activity throughout the reaction cycle.

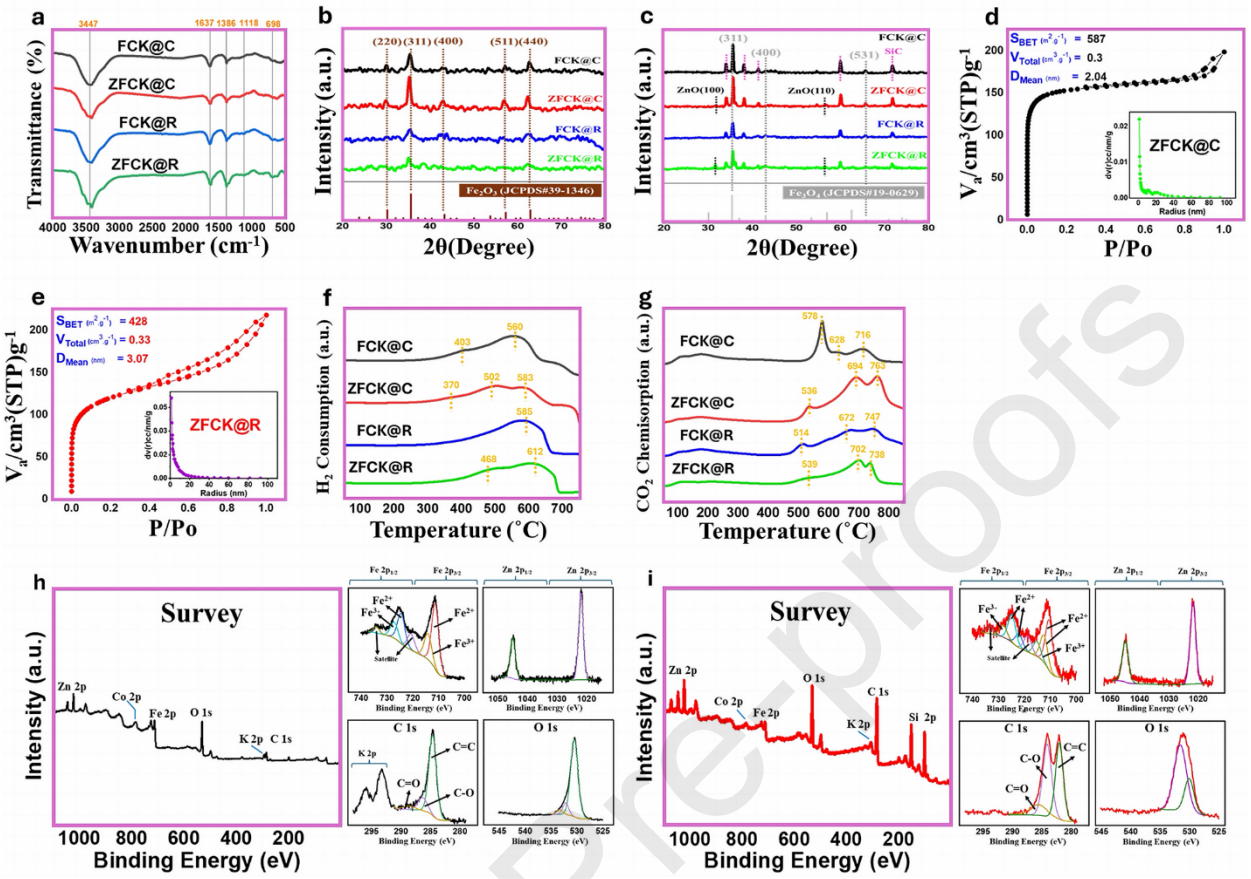

Fig. 4. (a) FTIR analysis, (b) XRD patterns of fresh catalysts, (c) XRD patterns of spent catalysts, (d) BET analysis of ZFCK@C, (e) BET analysis of ZFCK@R, (f) H_2-TPR profiles, (g) CO_2-TPD profiles, (h) XPS analysis of fresh ZFCK@C, (i) XPS analysis of spent ZFCK@C.

Fig. 5 depicts TEM images, EDS elemental mapping, and particle size distribution for the fresh FCK@C, ZFCK@C, FCK@R, and ZFCK@R samples. At a 5 nm magnification scale, all images show a consistent distribution of micropores that resemble a honeycomb pattern due to the porous nature of the carbonaceous supports within the catalysts. The average pore sizes for the catalysts were around 0.55 nm, as measured using ImageJ software. This uniform pore size is typical of carbonaceous materials, which frequently have closely spaced micropores. Aligning with this observation, Guo et al. [75] previously established that active carbon has a honeycomb-like structure with holes smaller than 2 nm, while Kumar and Jena [76] showed that activated carbon from fox nutshells had an average pore diameter of 0.64 nm. FCK@C, ZFCK@C, FCK@R and ZFCK@R have an average particle size of 34.7, 33.9, 35.8, and 34.6 nm, respectively. This demonstrates Zn's ability to reduce particle size. Smaller particles typically offer a higher surface area, which can enhance catalytic activity. In carbon-supported catalysts, crystal size from XRD and particle size from TEM can differ significantly because of the nature of these measurement techniques and the structure of carbon-based supports. XRD measures the size of individual metal crystallites based on coherent scattering domains, often resulting in smaller size measurements since it only captures well-ordered, crystalline regions. On the other hand, TEM provides an image of the entire particle, which may appear larger because it includes not only these crystalline domains but also any amorphous material in the sample—particularly relevant for carbonaceous

supports such as biochar or activated carbon, which often contain both crystalline and amorphous structures. All catalysts exhibit interlayer spacings of 0.25 nm, associated with the (311) plane of Fe_2O_3 as confirmed by the XRD results, suggesting an enhanced distribution of Fe species within the material. Elemental analysis via EDS confirms that all samples contain Fe, Co, K, and O; however, the Zn-containing sample, ZFCK@C, demonstrates the most uniform distribution of these components. This result highlights the role of Zn and biochar in promoting homogeneity, likely contributing to improved structural stability and catalytic performance.

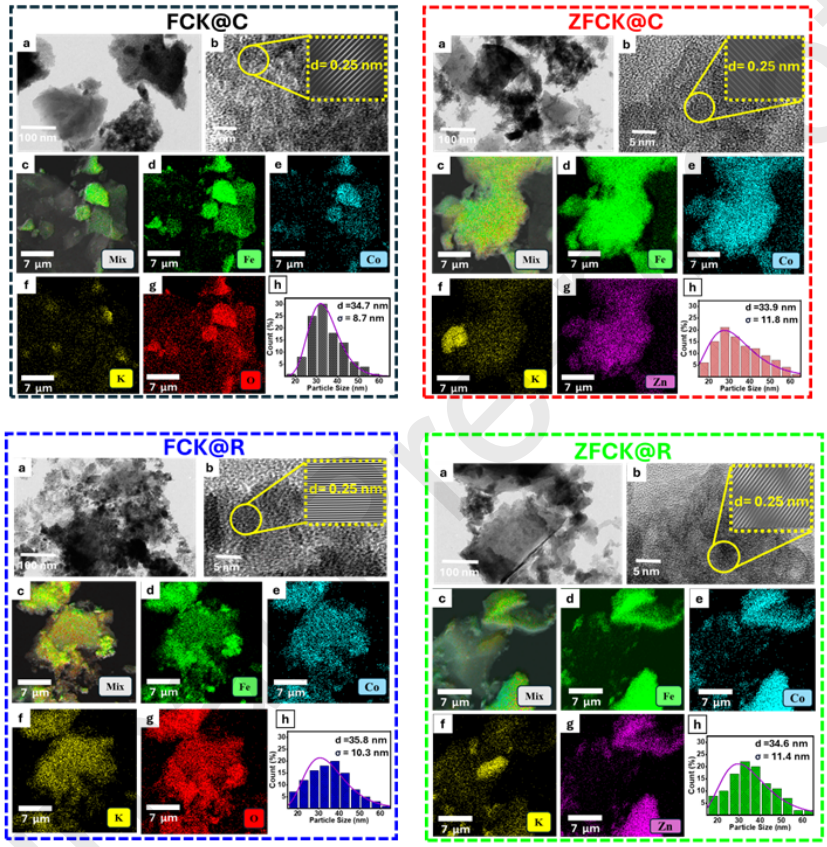

Fig. 5. TEM images with EDS mapping and particle size distribution of as-prepared catalysts.

The following section provides a detailed analysis of the CO and CO_2 hydrogenation test for the four catalyst samples (FCK@C, FCK@R, ZFCK@C, and ZFCK@R) highlighting key differences in their performance based on the presence of biochar, activated carbon, and Zn.

3.2. Evaluation of CO Hydrogenation Performance

Fig. 6a illustrates the CO conversion and selectivities for CO_2, CH_4, light hydrocarbons (C_2-C_4), and higher hydrocarbons (C_{5+}), with additional data on higher hydrocarbon and olefin (C_{5+}) yield and O/P ratio provided in Table S2. In the absence of Zn, both FCK@C and FCK@R catalysts achieve a CO conversion rate of approximately 92%. Among these, FCK@C stands out with a higher C_{5+} hydrocarbon selectivity of 32.1% compared to 20.7% for FCK@R. Additionally,

FCK@C achieves a lower CO_2 selectivity of 35.0%, compared to 40.4% for FCK@R. Upon the introduction of Zn, both ZFCK@C and ZFCK@R exhibited improved CO conversion rates exceeding 95%. However, this enhanced conversion is accompanied by a slight increase in CH_4 selectivity for both catalysts. ZFCK@C achieves a C_{5+} hydrocarbon selectivity of 32.2%. In

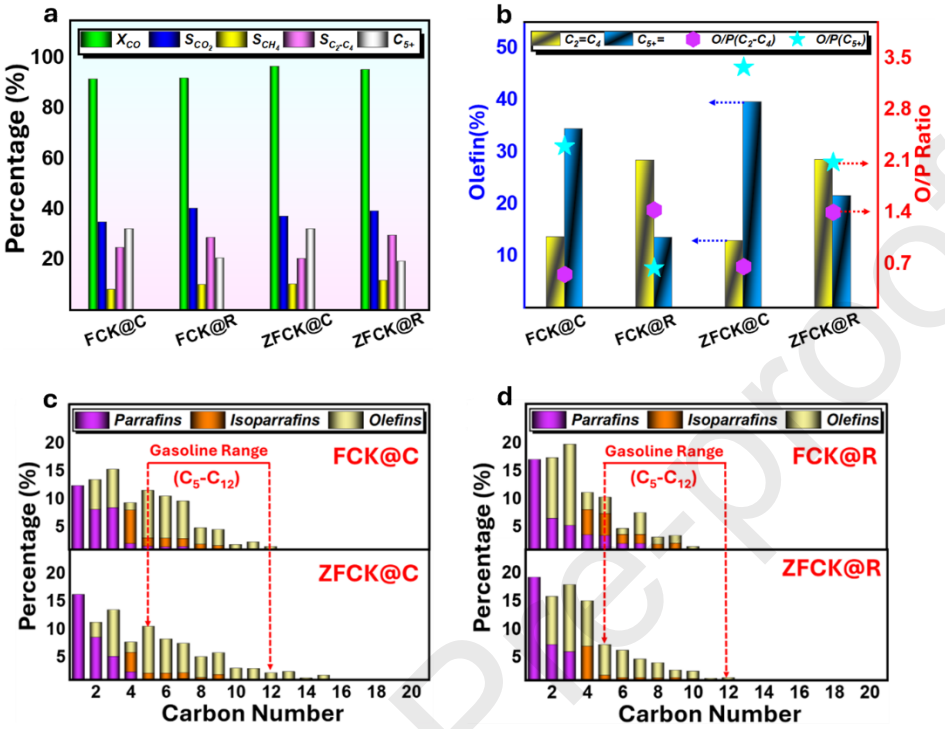

contrast, ZFCK@R shows a significantly higher selectivity for light hydrocarbons at 29.7%, compared to 20.3% for ZFCK@C. Fig. 6b highlights the superior performance of the FCK@C catalyst in terms of higher chain olefin (C_{5+}) distribution compared to FCK@R. FCK@C achieves olefin (C_{5+}) distribution of 34.4% with a yield of 20.5%, while FCK@R shows a significantly lower olefin (C_{5+}) distribution of 13.6% and a yield of 7.5%. This difference is reflected in the O/P ratio for C_{5+}, which rises dramatically from 0.64 for FCK@R to 2.3 for FCK@C. When Zn is introduced, ZFCK@C further excels, achieving the highest olefin (C_{5+}) distribution of 39.6% compared to 21.6% for ZFCK@R. This enhancement boosts the O/P ratio for C_{5+} from 2.1 for ZFCK@R to 3.4 for ZFCK@C. ZFCK@C also achieves the highest total O/P ratio of 4.0, demonstrating the significant role of Zn in optimizing the catalyst's performance and maximizing the production of higher olefins. Biochar-supported catalysts demonstrate a higher distribution of gasoline-range hydrocarbons, with FCK@C achieving 46.6% and ZFCK@C 45.3%, compared to the lower distributions seen with activated carbon-containing catalysts as shown in Table S5 and Fig. 6c, d. In brief, the biochar significantly influences product selectivity towards higher hydrocarbons and olefins. The presence of Zn further enhances conversion rates and olefin yields for both catalyst types. However, biochar-supported catalysts, particularly ZFCK@C, exhibit a more favorable selectivity towards longer hydrocarbons and a higher O/P ratio compared to activated carbon-supported catalysts. This improved performance is likely due to the higher surface area of biochar, which provides more active sites for the reaction.

Fig. 6. CO Hydrogenation Evaluation: (a) CO conversion and, selectivity of CO_2 and hydrocarbons, (b) Olefin distribution and O/P ratio, and (c, d) Carbon distribution by carbon number.

3.3. Evaluation of CO_2 Hydrogenation Performance

The CO_2 hydrogenation performance of biochar-supported and activated carbon-supported catalysts was evaluated at 20 bar and 30 bar. Detailed information can be found in Table S3 and Table S4. The CO_2 conversion rates and selectivities for CO and hydrocarbons at 20 bar and 30 bar are summarized in Fig. 7a, b. At 20 bar, the FCK@C catalyst achieves a CO_2 conversion rate of 35.2% and demonstrates a high selectivity for higher chain hydrocarbons (C_{5+}) at 33.5%, surpassing the activated carbon-supported FCK@R, which has a C_{5+} selectivity of 25.1%. Similarly, ZFCK@C shows a CO_2 conversion rate of 35.3% and a C_{5+} selectivity of 39.3%, compared to ZFCK@R's C_{5+} selectivity of 29.5%. At 30 bar, ZFCK@C further enhances performance with a CO_2 conversion rate of approximately 40.1%, a C_{5+} selectivity of around 45.0%, and a CH_4 selectivity of 6.1%. In contrast, ZFCK@R exhibits a lower C_{5+} selectivity of 38.2% and a higher CH_4 selectivity of 17.2%. The introduction of Zn is observed to decrease CO selectivity for both catalyst types. Fig. 7c, d presents the distribution of olefin products in both light and heavy fractions, along with their respective O/P ratios. As shown in Fig. 7c, at 20 bar, biochar-supported catalysts—FCK@C and ZFCK@C—demonstrate higher olefin (C_{5+}) distributions of 34.4% and 32.0%, respectively, compared to activated carbon-supported catalysts (FCK@R and ZFCK@R) which have distributions of 22.6% and 22.0%, respectively. Notably, FCK@C achieves the highest O/P(C_{5+}) ratio of 2.2. As pressure increases, the olefin distribution improves for all catalysts, as depicted in Fig. 7d. ZFCK@C reaches a maximum olefin(C_{5+}) distribution of approximately 39%, which results in an increased O/P(C_{5+}) ratio of approximately 2.2, highlighting its superior selectivity for higher olefins. As shown in Fig. 7e-h, for FCK@C, the distribution of C_4 hydrocarbons remains nearly constant as the pressure increases. This behavior can be attributed to thermodynamic and kinetic factors that stabilize intermediate-chain hydrocarbons under varying pressure conditions. In contrast, higher pressure promotes chain growth and secondary hydrogenation reactions, resulting in an increase in olefin content due to enhanced reactant availability. The selectivity for C_5 hydrocarbons decreases for both FCK@C and ZFCK@C as the pressure increases. This trend is likely due to a shift toward the formation of longer-chain hydrocarbons (C_{5+}), particularly C_8, C_9, and C_{10}. The increased pressure facilitates chain propagation, making the production of higher-chain hydrocarbons more favorable. Based on the fuel liquid hydrocarbon distribution reported in Table S5, biochar-supported catalysts, ZFCK@C and FCK@C, exhibit superior performance at 20 bar. Both catalysts demonstrate a significant gasoline range hydrocarbon distribution of around 48%, with a higher olefin content compared to paraffins and isoparaffins. At 30 bar, ZFCK@C shifts its distribution towards the kerosene range, achieving a maximum value of 45.3%.

When comparing the total O/P ratio across CO and CO_2 hydrogenation, distinct trends emerge depending on the catalyst and reaction conditions. For CO hydrogenation, the ZFCK@C catalyst achieved the highest total O/P ratio of 4.04, highlighting its superior ability to produce olefins over paraffins. This result is attributed to the role of Zn in promoting CO dissociation and enhancing chain growth processes that favor olefin formation. Furthermore, Zn's role in reducing the particle size of active Fe species increases the number of active sites, optimizing the hydrogenation environment for olefin production. In contrast, a different trend is observed during CO_2 hydrogenation. At 20 bar, the FCK@C catalyst achieved the highest total O/P ratio of 2.81, significantly outperforming ZFCK@C. This behavior can be attributed to the Zn-free catalyst's less efficient CO_2 activation, which favors olefin production due to weaker paraffin formation pathways. However, at 30 bar, the total O/P ratios for both FCK@C and ZFCK@C become comparable, with each achieving a value of 3.22. The increase in pressure likely enhances CO_2

conversion efficiency and shifts the reaction equilibrium toward olefin formation for both catalysts. For ZFCK@C, this result reflects the combined effects of improved CO_2 activation via Zn species and enhanced hydrogenation activity at higher pressure, which balances the O/P ratio to levels comparable with FCK@C.

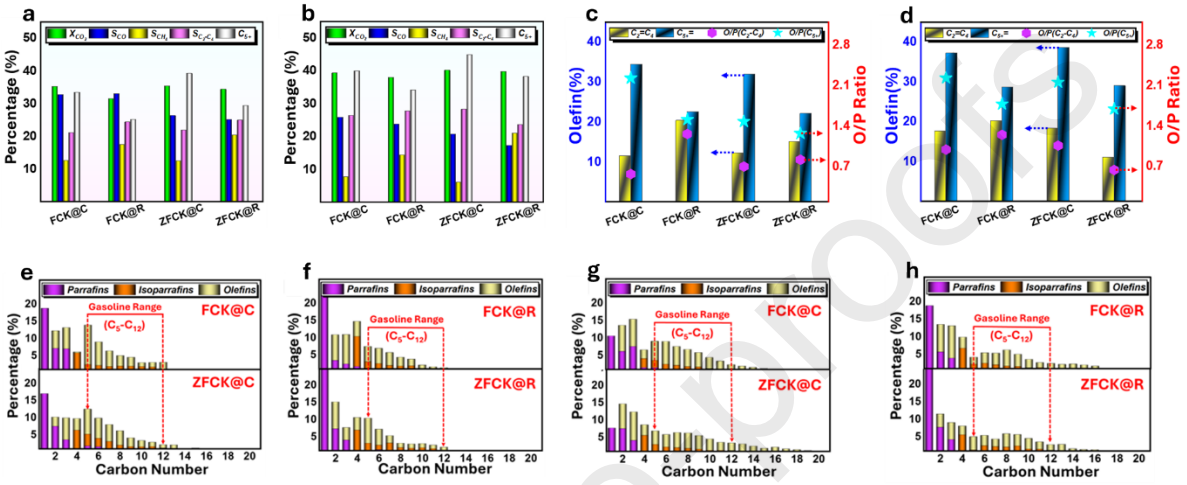

Fig. 7. CO_2 Hydrogenation Evaluation: CO_2 conversion and, selectivity of CO and hydrocarbons at (a) 20 bar and (b) 30 bar, Olefin distribution and O/P ratio at (c) 20 bar and (d) 30 bar, and Carbon distribution by carbon number at (e, f) 20 bar and (g, h) 30 bar.

Overall, the dual catalytic function of RWGS and FTS is essential for converting CO_2 and H_2 into valuable hydrocarbons. The Fe-based catalyst, though effective in the FTS reaction, shows high selectivity for CH_4. To address this, metals like Co and Zn are doped into the catalyst to improve the RWGS reaction efficiency. Biochar plays a pivotal role as a support material, significantly increasing the catalyst's surface area and providing additional active sites. As illustrated in Fig. 8, biochar facilitates CO_2 adsorption and the initial bond dissociation necessary for the RWGS reaction. In this process, biochar supports the breaking of the bond between one oxygen atom and the carbon atom, producing CO. This is followed by the dissociation of two hydrogen atoms and their recombination with oxygen to form water, completing the RWGS stage and setting the stage for the FTS process. During the FTS reaction, biochar aids in the secondary dissociation of the C-O bond, resulting in the formation of water. Concurrently, carbon atoms bond with hydrogen atoms to form CHx radicals. These radicals then combine with other CHx radicals, promoting the formation of longer hydrocarbon chains.

In summary, biochar's role in enhancing catalyst performance is significant. Its presence not only boosts the production of longer hydrocarbon chains and olefins but also directs the product distribution towards more valuable hydrocarbons in CO_2 hydrogenation reactions. This improvement is attributed to biochar's larger surface area and smaller pore diameter compared to activated carbon, as well as its higher CO_2 adsorption, which promotes more effective interactions and enhances overall catalyst efficiency.

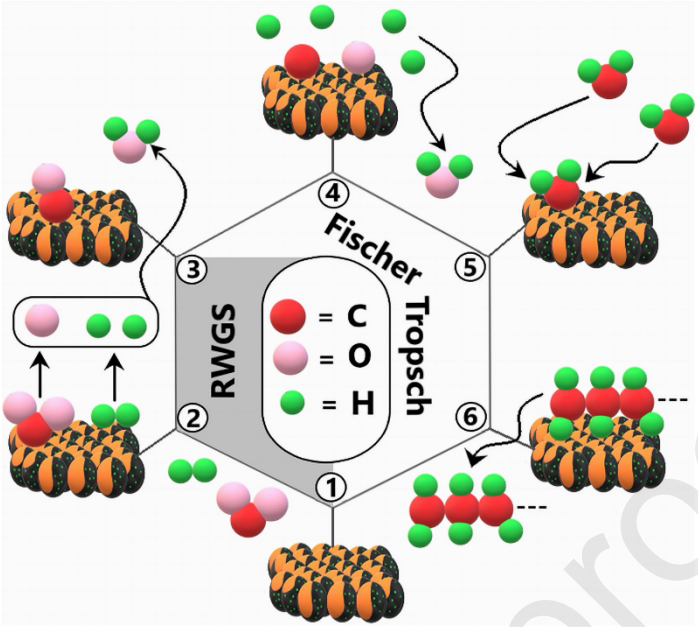

Fig. 8. Schematic illustration of dual catalytic functions: RWGS and FTS mechanisms for producing high chain hydrocarbons.

3.4. Evaluation of the Performance Stability

In the industrial sector, the long-term stability and activity of catalysts are vital. To test stability beyond 4 days, a series of continuous catalytic experiments were conducted, measuring ZFCK@C catalyst performance over time on stream (TOS), as shown in Fig. 9. After 100 h of operation, the catalyst remained effective and capable of functioning without showing any signs of deactivation. The catalytic performance, including conversion rate and C_1 selectivities, at the final stage was consistent with the initial stage under identical operating conditions, with a conversion rate difference of no more than ±1.0% for all reactions.

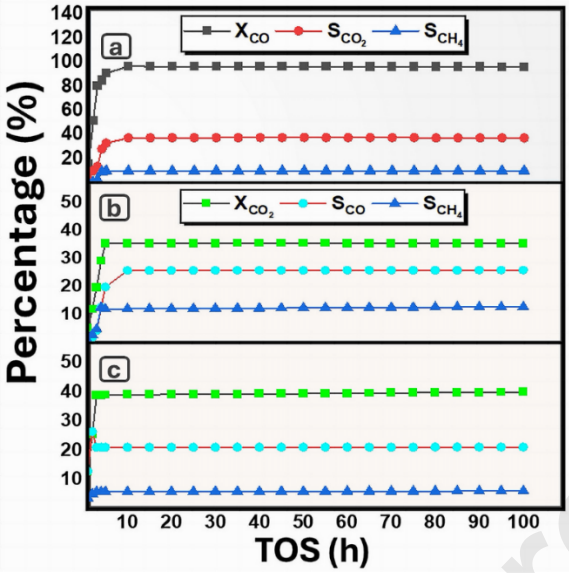

Fig. 9. Catalytic Performance Stability of ZFCK@C with a TOS of 100 h at 340 °C: (a) CO Hydrogenation at 20 bar, (b) CO_2 Hydrogenation at 20 bar, and (c) CO_2 Hydrogenation at 30 bar.

3.5. Comparative analysis with prior research

As shown in the comparative analysis in Table S6, CO hydrogenation was more efficient at temperatures above 300 °C, where catalysts with conversion rates over 90% typically had CO_2 selectivity around or above 40%. In this study, the ZFCK@C catalyst stood out with a conversion rate of approximately 97%, a lower CO_2 selectivity of 37%, and a higher selectivity for C_{5+} hydrocarbons at 32%. Additionally, ZFCK@C produced a notably high proportion of gasoline-range hydrocarbons, with a distribution of 45.3%.

Based on Table S7, it has been observed that carbon-supported Fe-based catalysts typically exhibit CO_2 conversion rates ranging from 30% to 40%. However, selectivity between light and heavy hydrocarbons varies significantly depending on the support material employed. For example, CNTs tend to favor the selectivity of light hydrocarbons, often at the expense of heavier hydrocarbons, while MOFs achieve higher conversion rates but are frequently associated with increased CH_4 selectivity. Although activated carbon supports reported in the literature generally demonstrate superior catalytic performance compared to other carbon supports, the ZFCK@C catalyst has achieved the best performance, with selectivity toward C_{5+} hydrocarbons reaching approximately 45.0% and attained a high kerosene distribution of 45.3%.

Unlike most previous studies that utilized micro-reactors and did not report the distribution of specific hydrocarbon ranges such as gasoline, kerosene, and diesel, this study stands out by employing a semi-industrial fixed-bed FTS reactor and offering a more detailed and practical analysis of hydrocarbon distribution. Additionally, while many FTS studies have used commercial activated carbon as a support, this work is unique in utilizing biochar derived from agricultural waste (corn cobs) through an environmentally friendly recycling process. The enhanced porous structure of the biochar-supported catalyst in this study led to higher production of C_{5+} hydrocarbons. This comparison is particularly significant, as the catalyst and operating conditions

were similar to previous research, with the exception of a difference in GHSV, highlighting the superior performance of the biochar-supported catalyst.

4. Conclusion

This study demonstrates the significant potential of industrial-scale synthesis in producing valuable liquid fuels through the hydrogenation of CO and CO_2. The research utilized biochar, produced via an eco-friendly recycling process from corn cobs, alongside commercial activated carbon as supports for Fe-based catalysts promoted with Co and K, with and without Zn. These catalysts were rigorously tested in a 1-inch semi-industrial fixed-bed FTS reactor designed to closely mimic industrial conditions. Notably, the ZFCK@C catalyst demonstrated exceptional performance, achieving a 97% conversion rate and a 45.3% distribution of gasoline-range hydrocarbons during CO hydrogenation at 20 bar and 340 °C. In CO_2 hydrogenation at 30 bar and 340 °C, it achieved a 40% conversion rate with a 45.3% distribution of kerosene-range hydrocarbons. The addition of Zn enhanced catalyst activity by increasing the electron density around Fe, providing more active sites, while the biochar support, with its high surface area, improved CO_2 adsorption efficiency on the catalyst surface. These findings collectively highlight a sustainable and practical approach to converting CO and CO_2 into high-value fuels, offering a promising solution to the environmental challenges posed by carbon emissions.

Acknowledgments

The authors gratefully acknowledge Dr. Ahmed Rashed for his exceptional support and valuable contributions throughout this work.

References

1. Sun, Y., W.J. Neary, Z.P. Burke, H. Qian, L. Zhu, and J.S. Moore, *Mechanically triggered carbon monoxide release with turn-on aggregation-induced emission.* Journal of the American Chemical Society, 2022. **144**(3): p. 1125-1129.

2. Stucki, D. and W. Stahl, *Carbon monoxide–beyond toxicity?* Toxicology letters, 2020. **333**: p. 251-260.

3. Zhou, P. and M. Wang, *Carbon dioxide emissions allocation: A review.* Ecological Economics, 2016. **125**: p. 47-59.

4. Siracusa, R., A. Schaufler, V. Calabrese, P.M. Fuller, and L.E. Otterbein, *Carbon monoxide: from poison to clinical trials.* Trends in pharmacological sciences, 2021. **42**(5): p. 329-339.

5. IEA., *Net Zero by 2050: A Roadmap for the Global Energy Sector.* Int. Energ. Agency, 2021. **224**.

6. Aresta, M., A. Dibenedetto, and A. Angelini, *Catalysis for the valorization of exhaust carbon: from CO2 to chemicals, materials, and fuels. Technological use of CO2.* Chemical reviews, 2014. **114**(3): p. 1709-1742.

7. Chen, X., D. Deng, X. Pan, Y. Hu, and X. Bao, *N-doped graphene as an electron donor of iron catalysts for CO hydrogenation to light olefins.* Chemical Communications, 2015. **51**(1): p. 217-220.

8. Satthawong, R., N. Koizumi, C. Song, and P. Prasassarakich, *Bimetallic Fe–Co catalysts for CO2 hydrogenation to higher hydrocarbons.* Journal of CO2 Utilization, 2013. **3**: p. 102-106.

9. Rodemerck, U., M. Holeňa, E. Wagner, Q. Smejkal, A. Barkschat, and M. Baerns, *Catalyst development for CO2 hydrogenation to fuels.* ChemCatChem, 2013. **5**(7): p. 1948-1955.

10. Owen, R.E., et al., *Shedding Light Onto the Nature of Iron Decorated Graphene and Graphite Oxide Nanohybrids for CO2 Conversion at Atmospheric Pressure.* ChemistryOpen, 2020. **9**(2): p. 242-252.

11. Herranz, T., S. Rojas, F.J. Pérez-Alonso, M. Ojeda, P. Terreros, and J.L.G. Fierro, *Carbon oxide hydrogenation over silica-supported iron-based catalysts: Influence of the preparation route.* Applied Catalysis A: General, 2006. **308**: p. 19-30.

12. Liu, J., A. Zhang, M. Liu, S. Hu, F. Ding, C. Song, and X. Guo, *Fe-MOF-derived highly active catalysts for carbon dioxide hydrogenation to valuable hydrocarbons.* Journal of CO2 Utilization, 2017. **21**: p. 100-107.

13. Kabir, L.M. and A. El-moneim, *Mof-Derived Cocu@ C Catalyst for Syngas Conversion to Synthetic Natural Gas Enriched with Natural Gas Liquids.* Available at SSRN 4887620.

14. Hwang, S.-M., et al., *Mesoporous carbon as an effective support for Fe catalyst for CO2 hydrogenation to liquid hydrocarbons.* Journal of CO2 Utilization, 2020. **37**: p. 65-73.

15. Chen, Y., et al., *Carbon-supported Fe catalysts with well-defined active sites for highly selective alcohol production from Fischer-Tropsch synthesis.* Applied Catalysis B: Environmental, 2022. **312**: p. 121393.

16. Nasser, A.-H., L. Guo, H. ELnaggar, Y. Wang, X. Guo, A. AbdelMoneim, and N. Tsubaki, *Mn–Fe nanoparticles on a reduced graphene oxide catalyst for enhanced olefin production from syngas in a slurry reactor.* RSC advances, 2018. **8**(27): p. 14854-14863.

17. El-Basaty, A., E. Moustafa, A. Fouda, and A. El-Moneim, *3D hierarchical graphene/CNT with interfacial polymerized polyaniline nano-fibers.* Spectrochimica Acta Part A: Molecular and Biomolecular Spectroscopy, 2020. **226**: p. 117629.

18. Eldesouki, M.H., A.E. Rashed, and A.A. El-Moneim, *A comprehensive overview of carbon dioxide, including emission sources, capture technologies, and the conversion into value-added products.* Clean Technologies and Environmental Policy, 2023. **25**(10): p. 3131-3148.

19. Koizumi, N., X. Jiang, J. Kugai, and C. Song, *Effects of mesoporous silica supports and alkaline promoters on activity of Pd catalysts in CO2 hydrogenation for methanol synthesis.* Catalysis today, 2012. **194**(1): p. 16-24.

20. Wei, J., J. Sun, Z. Wen, C. Fang, Q. Ge, and H. Xu, *New insights into the effect of sodium on Fe 3 O 4-based nanocatalysts for CO 2 hydrogenation to light olefins.* Catalysis Science & Technology, 2016. **6**(13): p. 4786-4793.

21. Liang, B., et al., *Effect of Na promoter on Fe-based catalyst for CO2 hydrogenation to alkenes.* ACS Sustainable Chemistry & Engineering, 2018. **7**(1): p. 925-932.

22. Han, Y., C. Fang, X. Ji, J. Wei, Q. Ge, and J. Sun, *Interfacing with carbonaceous potassium promoters boosts catalytic CO2 hydrogenation of iron.* ACS Catalysis, 2020. **10**(20): p. 12098-12108.

23. Wang, S., et al., *Iron–potassium on single-walled carbon nanotubes as efficient catalyst for CO2 hydrogenation to heavy olefins.* ACS Catalysis, 2020. **10**(11): p. 6389-6401.

24. Zhou, Y., et al., *Promotion effects of alkali metals on iron molybdate catalysts for CO2 catalytic hydrogenation.* Journal of Energy Chemistry, 2023. **85**: p. 291-300.

25. Sun, Z., X. Chen, F. Lu, L. Zhou, and Y. Zhang, *Effect of Rb promoter on Fe3O4 microsphere catalyst for CO2 hydrogenation to light olefins.* Catalysis Communications, 2022. **162**: p. 106387.

26. Wang, X., P.J. Ramírez, W. Liao, J.A. Rodriguez, and P. Liu, *Cesium-induced active sites for C–C coupling and ethanol synthesis from CO2 hydrogenation on Cu/ZnO (000$\bar{1}$) surfaces.* Journal of the American Chemical Society, 2021. **143**(33): p. 13103-13112.

27. Dongil, A.B., Q. Zhang, L. Pastor-Pérez, T. Ramírez-Reina, A. Guerrero-Ruiz, and I. Rodríguez-Ramos, *Effect of Cu and Cs in the β-Mo2C System for CO2 Hydrogenation to Methanol.* Catalysts, 2020. **10**(10): p. 1213.

28. Kapiamba, K.F., H.O. Otor, S. Viamajala, and A.C. Alba-Rubio, *Inverse oxide/metal catalysts for CO2 hydrogenation to methanol.* Energy & Fuels, 2022. **36**(19): p. 11691-11711.

29. Zhang, J., X. Su, X. Wang, Q. Ma, S. Fan, and T.-S. Zhao, *Promotion effects of Ce added Fe–Zr–K on CO 2 hydrogenation to light olefins.* Reaction Kinetics, Mechanisms and Catalysis, 2018. **124**: p. 575-585.

30. Ding, J., et al., *CO2 hydrogenation to light olefins with high-performance Fe0. 30Co0. 15Zr0. 45K0. 10O1. 63.* Journal of Catalysis, 2019. **377**: p. 224-232.

31. Liang, J., et al., *Direct conversion of CO2 to aromatics over K–Zn–Fe/ZSM-5 catalysts via a Fischer–Tropsch synthesis pathway.* Industrial & Engineering Chemistry Research, 2022. **61**(29): p. 10336-10346.

32. Malhi, H.S., C. Sun, Z. Zhang, W. Liu, P. Ren, W. Tu, and Y.-F. Han, *Catalytic consequences of the decoration of sodium and zinc atoms during CO2 hydrogenation to olefins over iron-based catalyst.* Catalysis Today, 2022. **387**: p. 28-37.

33. Liu, J., A. Zhang, X. Jiang, M. Liu, Y. Sun, C. Song, and X. Guo, *Selective CO2 hydrogenation to hydrocarbons on Cu-promoted Fe-based catalysts: dependence on Cu–Fe interaction.* ACS Sustainable Chemistry & Engineering, 2018. **6**(8): p. 10182-10190.

34. Nie, X., H. Wang, M.J. Janik, Y. Chen, X. Guo, and C. Song, *Mechanistic insight into C–C coupling over Fe–Cu bimetallic catalysts in CO2 hydrogenation.* The Journal of Physical Chemistry C, 2017. **121**(24): p. 13164-13174.

35. Peng, L., B. Jurca, A. Primo, A. Gordillo, V.I. Parvulescu, and H. García, *High C2-C4 selectivity in CO2 hydrogenation by particle size control of Co-Fe alloy nanoparticles wrapped on N-doped graphitic carbon.* Iscience, 2022. **25**(5).

36. Winter, L.R., E. Gomez, B. Yan, S. Yao, and J.G. Chen, *Tuning Ni-catalyzed CO2 hydrogenation selectivity via Ni-ceria support interactions and Ni-Fe bimetallic formation.* Applied Catalysis B: Environmental, 2018. **224**: p. 442-450.

37. Pandey, D. and G. Deo, *Determining the best composition of a Ni–Fe/Al2O3 catalyst used for the CO2 hydrogenation reaction by applying response surface methodology.* Chemical Engineering Communications, 2016. **203**(3): p. 372-380.

38. Aitbekova, A., et al., *Engineering of ruthenium–iron oxide colloidal heterostructures: Improved yields in CO2 hydrogenation to hydrocarbons.* Angewandte Chemie International Edition, 2019. **58**(48): p. 17451-17457.

39. Liang, B., et al., *Mn decorated Na/Fe catalysts for CO 2 hydrogenation to light olefins.* Catalysis Science & Technology, 2019. **9**(2): p. 456-464.

40. Baysal, Z. and S. Kureti, *CO2 methanation on Mg-promoted Fe catalysts.* Applied Catalysis B: Environmental, 2020. **262**: p. 118300.

41. Sun, Y., et al., *In Situ Hydrogenation of CO2 by Al/Fe and Zn/Cu Alloy Catalysts under Mild Conditions.* Chemical Engineering & Technology, 2019. **42**(6): p. 1223-1231.

42. Elishav, O., Y. Shener, V. Beilin, M.V. Landau, M. Herskowitz, G.E. Shter, and G.S. Grader, *Electrospun Fe–Al–O Nanobelts for Selective CO2 Hydrogenation to Light Olefins.* ACS Applied Materials & Interfaces, 2020. **12**(22): p. 24855-24867.

43. Landau, M.V., N. Meiri, N. Utsis, R. Vidruk Nehemya, and M. Herskowitz, *Conversion of CO2, CO, and H2 in CO2 Hydrogenation to Fungible Liquid Fuels on Fe-Based Catalysts.* Industrial & Engineering Chemistry Research, 2017. **56**(45): p. 13334-13355.

44. Gong, H., et al., *Fe-Sn bimetallic catalysts for an enhanced Fischer-Tropsch synthesis stability via oxygen removal and coking resistance.* Fuel, 2022. **311**: p. 122115.

45. White, R.J., V. Budarin, R. Luque, J.H. Clark, and D.J.J.C.S.R. Macquarrie, *Tuneable porous carbonaceous materials from renewable resources.* 2009. **38**(12): p. 3401-3418.

46. Hamed, A., A. Hessein, and A. Abd El-Moneim, *Towards high performance flexible planar supercapacitors: In-situ laser scribing doping and reduction of graphene oxide films.* Applied Surface Science, 2021. **551**: p. 149457.

47. Belal, M.A., H.H. Khalil, R.L. Mahajan, A.E. Rashed, S.N. Khattab, and A. Abd El-Moneim, *Layered structure design of inkjet-printed graphene/Co3O4 for high-performance flexible microsupercapacitors.* Journal of Energy Storage, 2024. **101**: p. 113900.

48. Rashed, A.E., A. Nasser, M.F. Elkady, Y. Matsushita, and A.A. El-Moneim, *Fe nanoparticle size control of the Fe-MOF-derived catalyst using a solvothermal method: effect on FTS activity and olefin production.* ACS omega, 2022. **7**(10): p. 8403-8419.

49. Cara, I.G., D. Țopa, I. Puiu, and G. Jităreanu, *Biochar a promising strategy for pesticide-contaminated soils.* Agriculture, 2022. **12**(10): p. 1579.

50. Xu, Z., M. He, X. Xu, X. Cao, and D.C. Tsang, *Impacts of different activation processes on the carbon stability of biochar for oxidation resistance.* Bioresource Technology, 2021. **338**: p. 125555.

51. Fan, M., et al., *Impact of biochar catalyst on pyrolysis of biomass of the same origin.* Journal of Environmental Chemical Engineering, 2022. **10**(5): p. 108546.

52. Wang, N., et al., *Comparative studies on Pb (II) biosorption with three spongy microbe-based biosorbents: High performance, selectivity and application.* Journal of hazardous materials, 2019. **373**: p. 39-49.

53. Eldesouki, M., Z. Abo-Shanab, M. El-Shafie, M. Abo-Riya, and S. El-Kholy, *Fabrication and evaluation of novel sulfur/epoxy resin composites.* Polymer Bulletin, 2023. **80**(11): p. 12047-12064.

54. Kaur, J., A.K. Sarma, M.K. Jha, and P. Gera, *Rib shaped carbon catalyst derived from Zea mays L. cob for ketalization of glycerol.* RSC advances, 2020. **10**(71): p. 43334-43342.

55. Mojoudi, N., N. Mirghaffari, M. Soleimani, H. Shariatmadari, C. Belver, and J. Bedia, *Phenol adsorption on high microporous activated carbons prepared from oily sludge: equilibrium, kinetic and thermodynamic studies.* Scientific Reports, 2019. **9**(1): p. 19352.

56. Eldesouki, M., Z. Abo-shanab, M. Mohammedy, M. Elshafie, M. Abo Riya, and S. Elkholy, *Evaluation of the dynamic mechanical analysis, water absorption and chemical resistance properties of sulfur/epoxy composites.* Egyptian Journal of Chemistry, 2021. **64**(1): p. 107-115.

57. Yu, X., et al., *Unlocking Dynamic Solvation Chemistry and Hydrogen Evolution Mechanism in Aqueous Zinc Batteries.* Journal of the American Chemical Society, 2024. **146**(25): p. 17103-17113.

58. Gao, X., J. Zhang, N. Chen, Q. Ma, S. Fan, T. Zhao, and N. Tsubaki, *Effects of zinc on Fe-based catalysts during the synthesis of light olefins from the Fischer-Tropsch process.* Chinese Journal of Catalysis, 2016. **37**(4): p. 510-516.

59. Jozwiak, W.K., E. Kaczmarek, T.P. Maniecki, W. Ignaczak, and W. Maniukiewicz, *Reduction behavior of iron oxides in hydrogen and carbon monoxide atmospheres.* Applied Catalysis A: General, 2007. **326**(1): p. 17-27.

60. Liang, M., W. Kang, and K. Xie, *Comparison of reduction behavior of Fe2O3, ZnO and ZnFe2O4 by TPR technique.* Journal of Natural Gas Chemistry, 2009. **18**(1): p. 110-113.

61. Ma, W. and A.K. Dalai, *Effects of structure and particle size of iron, cobalt and ruthenium catalysts on Fischer–Tropsch Synthesis.* Reactions, 2021. **2**(1): p. 62-77.

62. Han, Z., W. Qian, H. Zhang, H. Ma, Q. Sun, and W. Ying, *Effect of rare-earth promoters on precipitated iron-based catalysts for Fischer–Tropsch synthesis.* Industrial & Engineering Chemistry Research, 2020. **59**(33): p. 14598-14605.

63. Ali, J., et al., *Modulating the redox cycles of homogenous Fe (III)/PMS system through constructing electron rich thiomolybdate centres in confined layered double hydroxides.* Chemical Engineering Journal, 2021. **408**: p. 127242.

64. Ahmed, H.E., A.E. Rashed, M.E. El-Khouly, M.K. Albolkany, and A. Abd El-Moneim, *Green approach for sustainable production of paraffin fuel from CO2 hydrogenation on Fe-MOF catalyst.* Journal of Environmental Chemical Engineering, 2023. **11**(5): p. 111071.

65. Mohamed, M.M., E.E. Abdelmonem, and G. El-Sayed, *Unprecedented iron-based photoelectrocatalysts@ graphene foam composites as electrolyzing nanomaterials for water splitting in a neutral environment.* Journal of Photochemistry and Photobiology A: Chemistry, 2024. **447**: p. 115224.

66. Amin, M.O., B. D'Cruz, M. Madkour, and E. Al-Hetlani, *Magnetic nanocomposite-based SELDI probe for extraction and detection of drugs, amino acids and fatty acids.* Microchimica Acta, 2019. **186**: p. 1-10.

67. Chiu, N.-F., M.-J. Tai, D.T. Nurrohman, T.-L. Lin, Y.-H. Wang, and C.-Y. Chen, *Immunoassay-amplified responses using a functionalized mos2-based spr biosensor to detect Papp-a2 in maternal serum samples to screen for fetal down's syndrome.* International journal of nanomedicine, 2021: p. 2715-2733.

68. Lei, Y., J. Jiang, Y. Wang, T. Bi, and L. Zhang, *Structure evolution and stress transition in diamond-like carbon films by glancing angle deposition.* Applied Surface Science, 2019. **479**: p. 12-19.

69. Dolgov, A., D. Lopaev, C.J. Lee, E. Zoethout, V. Medvedev, O. Yakushev, and F. Bijkerk, *Characterization of carbon contamination under ion and hot atom bombardment in a tin-plasma extreme ultraviolet light source.* Applied surface science, 2015. **353**: p. 708-713.

70. Chen, X., X. Wang, and D. Fang, *A review on C1s XPS-spectra for some kinds of carbon materials.* Fullerenes, Nanotubes and Carbon Nanostructures, 2020. **28**(12): p. 1048-1058.

71. Ma, L., W. Xiang, H. Gao, J. Wang, Y. Ni, and X. Liang, *Facile synthesis of tunable fluorescent carbon dots and their third-order nonlinear optical properties.* Dyes and Pigments, 2016. **128**: p. 1-7.

72. Yang, S., H.-J. Chun, S. Lee, S.J. Han, K.-Y. Lee, and Y.T. Kim, *Comparative study of olefin production from CO and CO2 using Na-and K-promoted zinc ferrite.* ACS Catalysis, 2020. **10**(18): p. 10742-10759.

73. Pan, F., Y. Guo, F.-F. Cheng, T. Fa, and S.-D. Yao, *Synthesis of ZnFe2O4 nanomagnets by Fe-ion implantation into ZnO and post-annealing.* Chinese Physics B, 2011. **20**(12): p. 127501.

74. Jain, S., J. Shah, N.S. Negi, C. Sharma, and R.K. Kotnala, *Significance of interface barrier at electrode of hematite hydroelectric cell for generating ecopower by water splitting.* International Journal of Energy Research, 2019. **43**(9): p. 4743-4755.

75. Guo, H., Z. Liu, H. Li, H. Wu, C. Zhang, J. Yang, and X. Chen, *Active carbon electrode fabricated via large-scale coating-transfer process for high-performance supercapacitor.* Applied Physics A, 2017. **123**(7): p. 467.

76. Kumar, A. and H.M. Jena, *Adsorption of Cr(VI) from aqueous phase by high surface area activated carbon prepared by chemical activation with ZnCl2.* Process Safety and Environmental Protection, 2017. **109**: p. 63-71.

Highlights

- Iron-based catalysts supported on carbonaceous materials and promoted with Co, K, and/or Zn were evaluated for CO and CO_2 hydrogenation to gasoline-range hydrocarbons.
- Biochar support outperformed commercial activated carbon, by reducing CH_4 selectivity and increasing C_{5+} hydrocarbon production.
- A conversion rate of 97% was achieved in CO hydrogenation.
- Zinc promotion played a key role in boosting higher-chain hydrocarbon production.
- A stability test confirmed that ZFCK@C maintains stable activity after 100 h of reaction.